Small Angle Neutron Scattering Study of Nanoscale Structure of Low-Carbon Steel After Rolling with Shear Followed by Cold Drawing

Article *in* Metals and Materials International · June 2020

DOI: 10.1007/s12540-020-00766-x

Anatoliy Zavdoveev
E.O. Paton Electric Welding Institute

Metals and Materials International
https://doi.org/10.1007/s12540-020-00766-x

Small Angle Neutron Scattering Study of Nanoscale Structure of Low-Carbon Steel After Rolling with Shear Followed by Cold Drawing

Anatoliy Zavdoveev[1] · A. Len[2,3] · E. Pashinska[4]

Received: 16 March 2020 / Accepted: 10 May 2020

Abstract
Small angle neutron scattering was applied to steel produced by rolling with shear (RS) technology and compared to samples produced by standard technology (ST). Based on small angle neutron scattering measurements the morphology of the grains and pores of RS steels were compared to those of the ST steels. The scattering in small scattering vector region showed anisotropy, attributed to the elongation of the pores; the pearlite lamellae distances along and perpendicular to the rolling directions differed by a factor of 1.5. The results of the Small angle neutron scattering measurements were in accordance with the electrical characteristics of the specimens. They showed smaller and less anisotropic average sizes of the cracks and nanopores for the RS samples than for the ST rods. This confirms the dynamic healing of the nanosized defects during the cold drawing of the RS rods. This fundamental result shows that during severe plastic deformation a cyclic process of nucleation and healing of the nanovoids took place. However, during the standard deformation process only nucleation of the nanovoids is present.

Keywords Low carbon steel · Nanostructure · SANS · Rolling with shear · Severe plastic deformation

1 Introduction

Severe plastic deformation (SPD) of metals has become an important method for forming ultrafine grained structures [1–8]. As shown in our earlier work [9], SPD is a type of deformation which develops under the simultaneous action of several forces and moments of force. The materials obtained by SPD are characterized by a unique complex of properties [10–12], such as high strength and ductility. The rolling with shear (RS) is a new continuous SPD method which is applicable for steel treatment [9]. High tensile wires have lower breakage rate, which reduces expenses for rod processing, and can be produced by the rolling combined with intermediate softening annealing, that additionally increases the plasticity. However, the annealing increases the cost of processing, and makes production more complex. The rolling with shear RS-technology ensures high plasticity of the material without the need of an intermediate annealing, and without decreasing the strength of the material.

Several works in the literature suggest that such deformations form bulk materials free of pores, but theoretical models show that micro and nanostructural defects are introduced during SPD [2, 9, 13–15]. This leads to fundamental limits in the enhancements achieved by the SPD process.

Scanning Electron Microscope (SEM) and transmission electron microscope (TEM) techniques are adequate to give information about the existence of sub-micron and nano-voids, however, we would like to know if such voids are introduced during the fracture process of the sample preparation [16]. Therefore, in this study we used the non-destructive method of small angle neutron scattering

This paper is dedicated to the memory of Prof. János Füzi, who passed away in January 2020.

✉ Anatoliy Zavdoveev
avzavdoveev@gmail.com

1 Welding of alloyed steels, Paton Electric Welding Institute of NAS of Ukraine, Kiev 03680, Ukraine

2 Neutron Spectroscopy Department, Centre for Energy Research, Budapest 1121, Hungary

3 Faculty of Engineering and Information Technology, University of Pécs, Pecs 7624, Hungary

4 High-pressure physics and advanced technology, Donetsk Institute for Physics and Engineering Named After A.A. Galkin of the NAS of Ukraine, Kiev 03028, Ukraine

Published online: 16 June 2020

(SANS) to clarify the origin of voids, cracks and pores. The main objective of this contribution is to study the correlation between the nanostructure of low-carbon steel after SPD together with its physical and mechanical characteristics in order to contribute to the knowledge about processing using cold drawing.

2 Materials and Methods

2.1 Processing Technology

The studied material consisted of commercial grade low-carbon steel of nominal chemical composition as shown in Table 1.

The processing consisted of rolling and cold drawing [14, 17–19]. In the case of the ST-technology, after the rolling, a cold drawing was applied and a rod with diameter of 6.5 mm was obtained. The drawing was continued at ambient temperature, however before reaching the 3.4 mm diameter the loss of ductility was observed and several cracks got introduced in the material texture. Therefore an intermediate softening annealing, carried out in a tube furnace at a temperature of 600 °C for 1 h, with air cooling, was applied. After this, the cold drawing could be continued until the diameter of 2.3 mm was reached. In the case of the RS-technology, the rod of 9.15 mm in diameter was drawn at ambient temperature to 1.55 mm, without the need of any intermediate softening annealing.

The internal structure of the investigated steel was visualized by electron backscatter diffraction (EBSD) and TEM. It is seen that after hot rolling with shear, the structure of low-carbon steel is finer, and more uniform compared with using standard hot rolling (Fig. 1a, b). This is a consequence and feature of the deformation scheme. For a more detailed analysis a TEM investigation was also carried out (Fig. 1c, d). The TEM images reveal the triple junction of ferrite grains. In the case of RS-technology the bulk of the ferrite grains are free from the dislocations observed during standard rolling.

2.2 Small Angle Neutron Scattering (SANS)

The samples (Fig. 2) measured by SANS [20] were chosen from the different steps of the drawing. In each case the sample thickness was limited to maximum 2 mm (this was reached through machining), in order to reduce multiple scattering. The original diameters were: 6.5 mm, 5 mm, 3 mm, and 2 mm.

In a SANS measurement the neutrons, scattered in angles smaller than 10 degrees, are detected on a position sensitive detector. The scattering angle (θ) and the incoming neutron wavelength (λ) define the Q scattering vector: $Q = (4\pi/\lambda)\sin(\theta/2)$. After the instrumental calibration (background

Table 1 Chemical composition of the low-carbon steel in wt%

C	Mn	Si	S	P	Cr	Ni	Cu	N
0.08	1.87	0.82	0.020	0.022	0.02	0.02	0.02	0.007

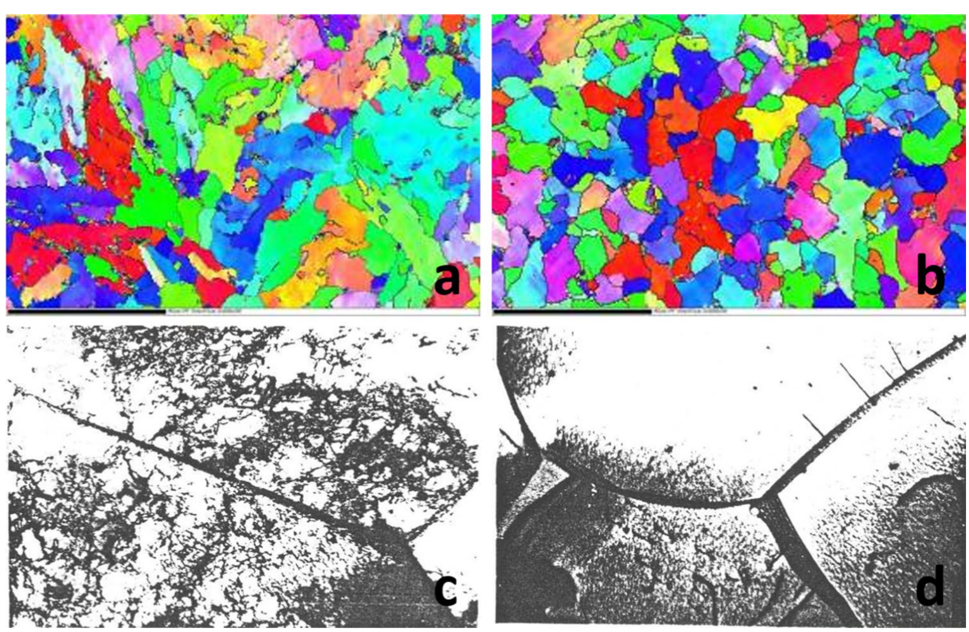

Fig. 1 Microstructure of the investigated steel: **a**, **c** ST; **b**, **d** RS. **a**, **b** EBSD orientation maps; **c**, **d** TEM, ×20000

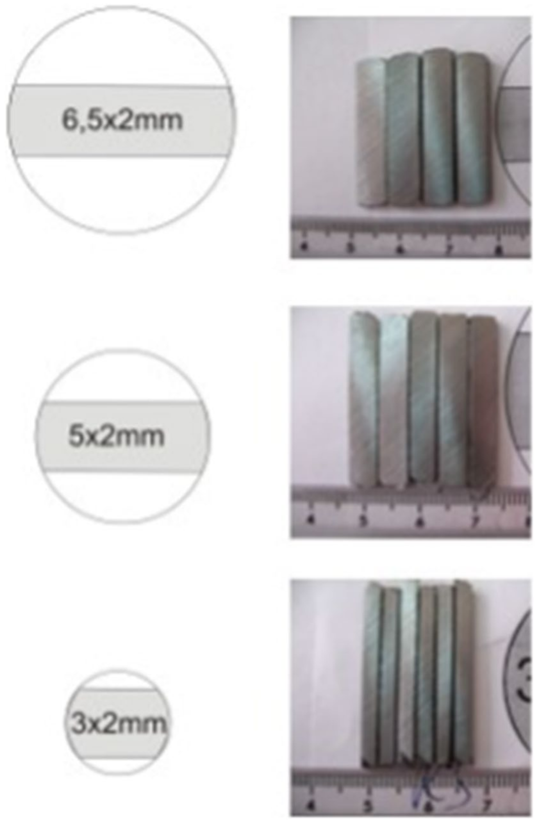

Fig. 2 Scheme of the samples machining

noise, detector pixel sensitivity) the detected neutron intensity is plotted versus the scattering vector. If the scattering is anisotropic (see Fig. 1), different, usually vertical and horizontal sectors of the scattering intensity maps are chosen and the intensities are radially averaged inside the sector and plotted versus the scattering vector.

The scattering curves contain information about the morphology of the scattering objects, which are nanometre sized regions in which the neutron scattering length density differs from that in their surroundings. By SANS useful information can be obtained about the shape, size, size-distribution, orientation, surface characteristics of the scattering objects, which is averaged over the total volume of the sample placed into the neutron beam. There is no need of special sample preparation that could introduce unwanted artefacts in the microstructure.

Samples processed with standard ST-technology and with rolling with shear RS-technology have been measured at the Yellow Submarine SANS spectrometer at the Budapest Neutron Centre. Yellow Submarine is a pin-hole type SANS instrument equipped with a 64 × 64 pixel BF_3 detector (pixel size: 1 cm^2). The used sample to detector distances were 1.3 m and 5.4 m, and the used wavelengths were 3.7 Å and 8.5 Å with 20% wavelength spread. The samples were placed in

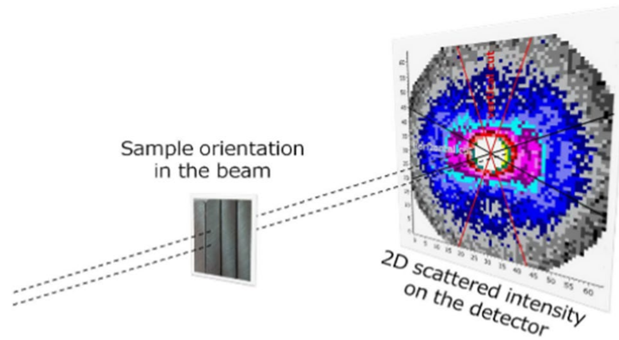

Fig. 3 Sample orientation in the beam

the neutron beam as shown in Fig. 3. The rods were aligned vertically, and the scattering intensity was analysed in horizontal and vertical sectors of the registered 2D scattering data. The whole available Q range was 0.007–0.4 $Å^{-1}$. The registered 2D scattering intensities for the samples with 6.5 mm original diameter are shown in Fig. 4.

2.3 Conductivity Measurements

The conductivity of the rod samples was measured by the standard four-probe method. The distance between current contacts significantly exceeded the distance between the potential contacts. In this case, a condition was provided under which the equipotential surfaces in the region of potential contacts were almost flat and perpendicular to the axis of the samples. High accuracy in determining the specific conductivity (error not more than 0.1%) was also ensured by the stability of the wire diameter along the entire length of the samples for greater accuracy in measuring all parameters and calculating the conductivity [21].

3 Results and Discussion

The SANS curves were analysed separately in the low Q part (0.007–0.05 $Å^{-1}$) with the aid of Eq. (1), and the large Q part (0.05–0.4 $Å^{-1}$) was fitted by the sum of a Gaussian peak function and a power law function (2).

$$I(Q) = C1 \cdot exp\left(\frac{-Q^2Rg^2}{3}\right) + C2 \cdot \left(\frac{Q}{\mathrm{erf}(QRg/\sqrt{6})}\right)^{-p1} + bkg, \tag{1}$$

$$I(Q) = C3 \cdot Q^{-p2} + C4 \cdot \exp\left[-\left(\frac{Q - Q_0}{width}\right)^2\right] + bkg. \tag{2}$$

The first term of Eq. (1) is the Guinier equation, describing the size of scattering objects, where Rg is the gyration radius, the second term describes the scattering from large

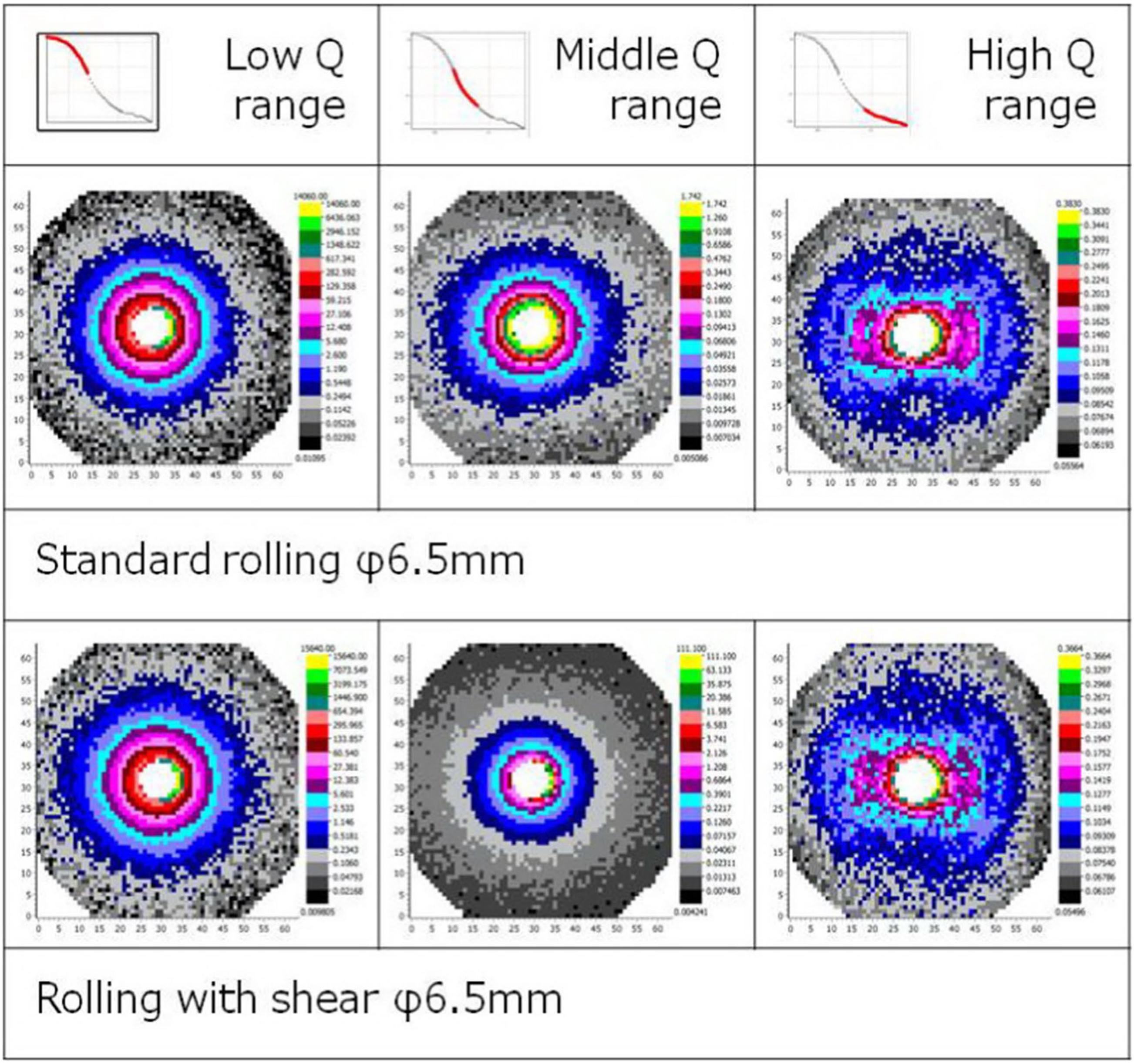

Fig. 4 2D scattering maps of the ST and RS samples (diameter of 6.5 mm) at three different Q ranges

grain surfaces. p1 and p2 are related to the surface characteristics of the scattering interfaces [22].

The strongly anisotropic distribution of the scattering intensity along vertical and horizontal directions shows the corresponding anisotropy of the structure, which is induced by the drawing process. The inhomogeneities in the material can be approximated as anisotropic objects, having elongated shapes with their long axes aligned along the direction of drawing. In such cases horizontal and vertical cuts of the anisotropic SANS patterns can be treated separately. The 1D scattering curves obtained by radial averaging, the intensities in the horizontal and vertical sectors of the 2D scattering pattern, correspond to the apparent dimensions of these objects along or perpendicular to the drawing direction, respectively (Fig. 5), if the samples (and the scattering objects) are aligned in the neutron beam with their long axis placed vertically (see Fig. 3). Tables 1 and 2 contain the values of the fitted parameters for ST and RS samples for the horizontal and vertical cuts, respectively.

The Guinier type scattering is attributed mainly to the nanometric sized pores, cracks and defects, or crystallites and precipitates. For our materials it can be assumed that the mechanical treatment mostly modified the voids, therefore the observed microstructural changes (elongation) can

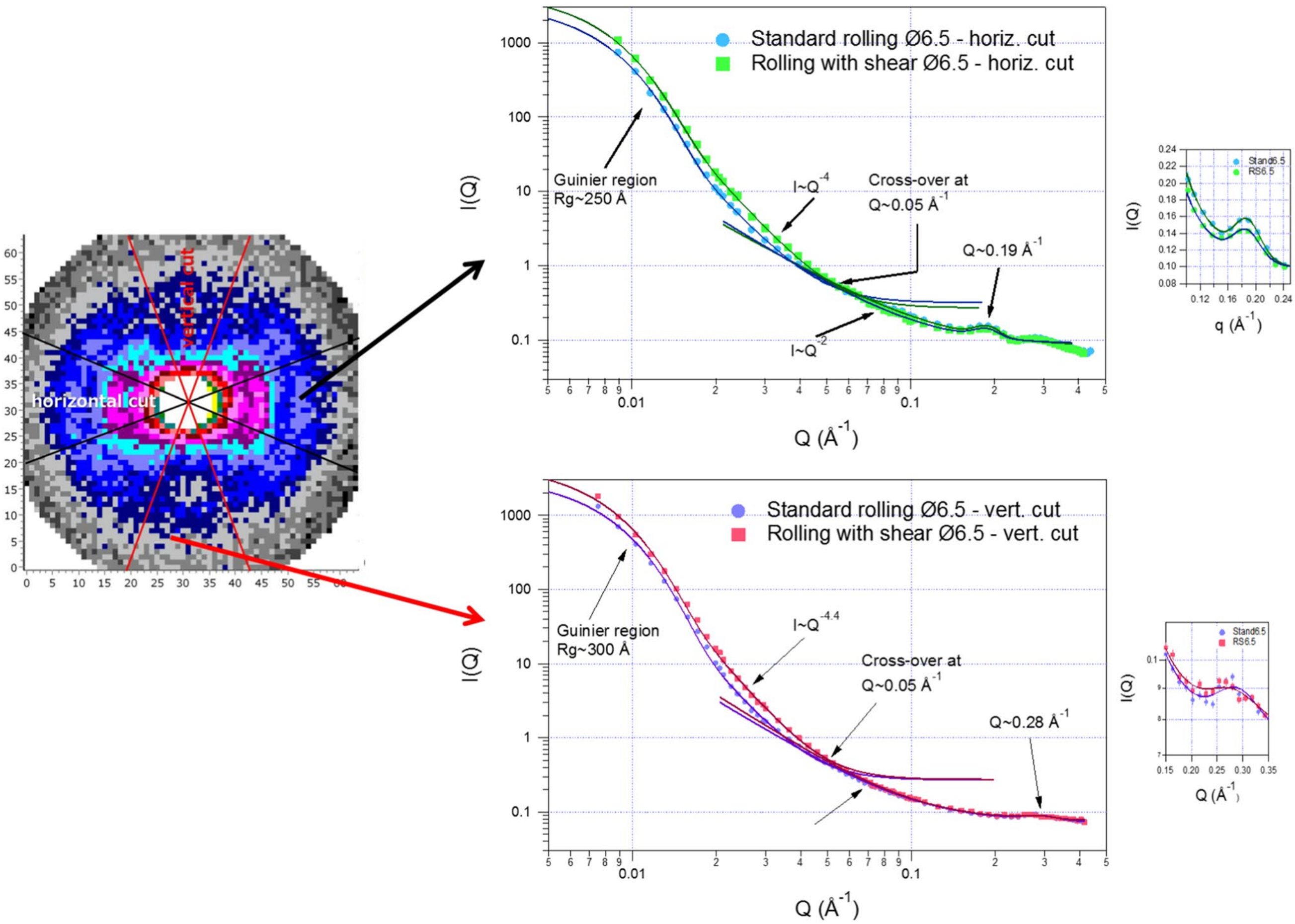

Fig. 5 Horizontal and vertical cuts from the 2D scattering map for the ST and RS samples with 6.5 mm diameter. Symbols represent the measured data, while lines the fitted models

Table 2 Fitting parameters for the horizontal cut for the samples processed with ST and RS technologies

Sample	Rod diameter (mm)	Rg (Å)	P1	Repeating distance (Å)	P2
ST6.5	6.5	252 ± 1	4.0 ± 0.04	33.4 ± 0.2	2.1 ± 0.2
ST5	5	271 ± 1	4.0 ± 0.1	34.2 ± 0.2	1.6 ± 0.5
ST3	3	282 ± 1	4.5 ± 0.1	33.4 ± 0.5	1.0 ± 0.5
ST2	2	286 ± 1	4.6 ± 0.1	34.3 ± 0.6	1.5 ± 0.8
RS6.5	6.5	250 ± 1	4.1 ± 0.03	33.6 ± 0.4	2.3 ± 0.3
RS5	5	261 ± 1	4.2 ± 0.1	33.8 ± 0.4	1.8 ± 0.4
RS3	3	260 ± 1	4.2 ± 0.04	33.1 ± 0.5	1.8 ± 0.4
RS2	2	262 ± 1	4.8 ± 0.1	33.4 ± 0.5	1.3 ± 0.7

Table 3 Fitting parameters for the vertical cut for the samples processed with ST and RS technologies

Sample	Rod diameter (mm)	Rg (Å)	p1	Repeating distance (Å)	p2
ST6.5	6.5	245 ± 1	4.2 ± 0.02	21.7 ± 0.2	2.6 ± 0.01
ST5	5	286 ± 1	4.5 ± 0.03	20.5 ± 0.7	2.4 ± 0.01
ST3	3	313 ± 1	5.2 ± 0.03	–	2.6 ± 0.02
ST2	2	362 ± 2	5.4 ± 0.03	21.1 ± 0.5	2.8 ± 0.03
RS6.5	6.5	252 ± 1	4.4 ± 0.02	22.4 ± 0.4	3.0 ± 0.01
RS5	5	283 ± 1	4.6 ± 0.03	21.8 ± 0.4	2.5 ± 0.01
RS3	3	316 ± 1	5.0 ± 0.03	–	2.8 ± 0.02
RS2	2	331 ± 2	5.7 ± 0.04	21.7 ± 0.5	2.6 ± 0.03

be associated with the changes of the pore size, shape and quantity.

In the large Q region, a marked scattering peak is visible which corresponds to the repeat distance of the perlite grains, along and perpendicular to the drawing directions (Fig. 5). These grains are oriented parallel to the rod axis, producing a strongly anisotropic scattering pattern. The repeat distances of the ferrite and iron-carbide layers, determined as $d = 2\pi/Q$, are about 2 nm and 3 nm, respectively, along and perpendicular to the drawing direction (Tables 2, 3). They are slightly larger for the RS samples, which can be attributed to different deformation degrees of the pearlite grains or dynamic recovery processes.

Figure 6 shows the evolution of the void sizes in the samples processed with standard rolling and rolling with shear. The average size of the defects is lower for both—horizontal and vertical—directions in the case of RS technology, and the sizes increase with the decreasing rod diameter.

Figure 7 shows the evolution of specific conductivity and density for ST and RS processed samples. It can be seen that with increasing deformation (decreasing of the rod diameter), the conductivity as well as density for the ST sample continuously decreased, while for RS samples there is a region of saturation with a nearly constant level. This correlates with the data obtained for gyration radii (Fig. 6), where the average radius of nanopores for the RS samples also shows saturation. Meanwhile, the gyration radii for the ST sample is continuously increasing, which affects the behaviour of the specific conductivity.

The presented data show that in rods prepared with RS technology the dynamic healing of the nanovoids can be followed with structural characterization by scattering methods. The RS method provides good plasticity and higher specific conductivity, showing effectiveness of RS technology in producing rods with high performance [14, 23].

4 Conclusions

The development of the nanostructure with the progress of the processing of low carbon steel rods has been investigated by small-angle neutron scattering. A significant structural difference at nanoscale level between the ST and RS processed samples was revealed. The average size of the voids and defects increased with the decrease of the rod diameter for both technologies. Application of RS technology resulted in elongated nanometric sized voids, proven by the anisotropy increase in the 2D scattering patterns. The average sizes of these defects as well as their aspect ratios were determined by applying suitable model analysis.

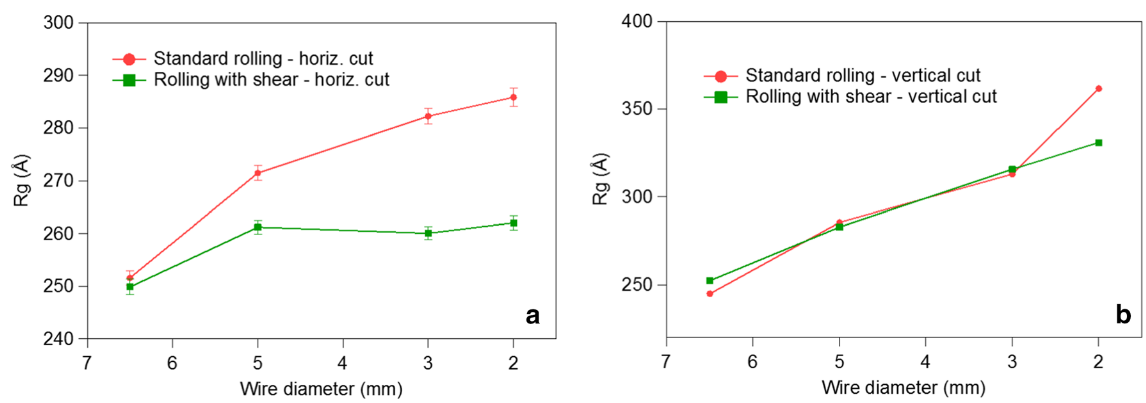

Fig. 6 **a** Change of the gyration radii along and **b** perpendicular to the drawing direction with the decreasing rod diameter for the ST and RS samples

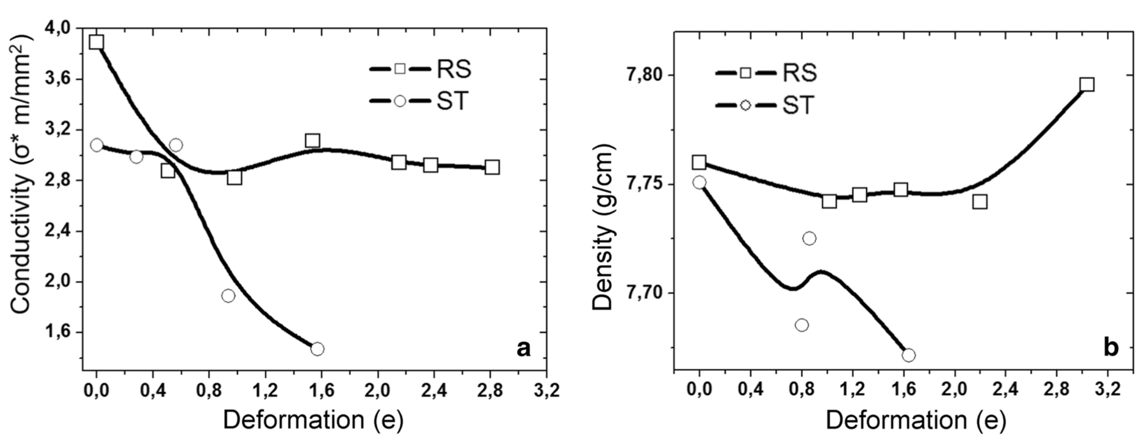

Fig. 7 Change of the specific conductivity **a** and density **b** for ST and RS samples. *e*—equivalent deformation

The observed changes in the microstructure correlate with the change of the specific conductivity of the RS samples. The evolution of the morphology in terms of gyration radii and the specific conductivity for RS samples show saturation behaviour. This is attributed to the nucleation and healing of the nanovoids in the cyclic process during SPD with RS processing, while during the standard deformation process only nucleation of nanovoids takes place.

Acknowledgements The research work reported in this paper was funded by the National Academy of Sciences of Ukraine—Young researchers grant No. 104. The authors are grateful to Dr. M. Heaton, Dr. Y. Nepochatov, A. Maksakova, B. Stebletsov, Gy. Káli and L. Almásy for help in experiments and preparation of the manuscript.

Data Availability The raw/processed data required to reproduce these findings can be requested from the authors.

Compliance with Ethical Standards

Conflict of interest A. Len, A. Zavdoveev, E. Pashinska declare that they have no conflict of interest.

References

1. Y. Estrin, A. Vinogradov, Acta Mater. **61**, 782–817 (2013)
2. H.S. Kim, Y. Estrin, M.B. Bush, Acta Mater. **48**, 493–504 (2000)
3. S.M. Alavizadeh, K. Abrinia, A. Parvizi, Met. Mater. Int. **26**, 260–271 (2020)
4. I.V. Ivanov, D.V. Lazurenko, A. Stark, F. Pyczak, A. Thömmes, I.A. Bataev, Met. Mater. Int. **26**, 83–93 (2020)
5. M. Zabihi, E. Emadoddin, F. Qods, Met. Mater. Int. **26**, 1–13 (2020)
6. H.S. Kim, M.H. Seo, S.I. Hong, Mater. Sci. Eng., A **291**, 86–90 (2000)
7. H.H. Lee, J.I. Yoon, H.S. Kim, Scr. Mater. **146**, 204–207 (2018)
8. H.H. Lee, J.I. Yoon, H.K. Park, H.S. Kim, Acta Mater. **166**, 638–649 (2019)
9. E. Pashinska, V. Varyukhin, A. Len, A. Zavdoveev, in: Proceedings of the "Condensed Matter Paris" 24–29th August, 2014, Paris, Fr., Paris, 2014
10. R.Z. Valiev, Met. Mater. Int. **7**, 413–420 (2001)
11. S. Takaki, T. Tsuchiyama, K. Nakashima, H. Hidaka, K. Kawasaki, Y. Futamura, Met. Mater. Int. **10**, 533–539 (2004)
12. N. Forouzanmehr, H.R. Jafarian, M. Samadi-khoshkhoo, M. Bönisch, M. Nili-Ahmadabadi, Met. Mater. Int. (2020). https://doi.org/10.1007/s12540-019-00575-x
13. Y. Beygelzimer, Mech. Mater. **37**, 753–767 (2005)
14. E. Pashinska, V. Varyukhin, M. Myshlaev, A.V. Zavdoveev, Adv. Eng. Mater. **16**, 26 (2014)
15. A. Vinogradov, Adv. Eng. Mater. **17**, 1710–1722 (2015)
16. R. Lapovok, D. Tomus, J. Mang, Y. Estrin, T.C. Lowe, Acta Mater. **57**, 2909–2918 (2009)
17. T. Brlić, S. Rešković, I. Jandrlić, Met. Mater. Int. **26**, 179–187 (2020)
18. S. Amani, G. Faraji, Met. Mater. Int. **25**, 1341–1359 (2019)
19. S.S. Gvk, M.J. Tan, Z. Liu, Met. Mater. Int. **25**, 1047–1062 (2019)
20. M. Wang, H.N. Han, H.-S. Chung, Y.-B. Chun, J. Jang, Met. Mater. Int. **25**, 140–146 (2019)
21. E.G. Pashinskaya, A.V. Zavdoveev, L.S. Metlov, Y.I. Nepochatikh, A.A. Maksakova, V.M. Tkachenko, Mater. Phys. Mech. **24**, 2 (2015)
22. A. Len, P. Harmat, G. Pépy, L. Rosta, Appl. Phys. A **74**, s1418–s1420 (2002)
23. E. Pashinska, V. Varyukhin, S. Dobatkin, A. Zavdoveev, Emerg. Mater. Res. **2**, 138–143 (2013)